Monthly Notices
of the
ROYAL ASTRONOMICAL SOCIETY

MNRAS **437,** 532–546 (2014)
Advance Access publication 2013 October 30

doi:10.1093/mnras/stt1906

Herschel SPIRE and PACS observations of the red supergiant VY CMa: analysis of the molecular line spectra*

Mikako Matsuura,[1]† J. A. Yates,[1] M. J. Barlow,[1] B. M. Swinyard,[1,2] P. Royer,[3] J. Cernicharo,[4] L. Decin,[3] R. Wesson,[1,5] E. T. Polehampton,[2,6] J. A. D. L. Blommaert,[3] M. A. T. Groenewegen,[7] G. C. Van de Steene[7] and P. A. M. van Hoof[7]

[1]*Department of Physics and Astronomy, University College London, Gower Street, London WC1E 6BT, UK*
[2]*Space Science and Technology Department, Rutherford Appleton Laboratory, Didcot, Oxfordshire OX11 0QX, UK*
[3]*Instituut voor Sterrenkunde, Katholieke Universiteit Leuven, Celestijnenlaan 200D, B-3001 Leuven, Belgium*
[4]*Laboratory of Molecular Astrophysics, Department of Astrophysics, CAB, INTA-CSIC, Ctra de Ajalvir, km 4, E-28850 Torrejón de Ardoz, Madrid, Spain*
[5]*European Southern Observatory, Alonso de Cordova 3107, Casilla 19001, Santiago, Chile*
[6]*Department of Physics and Astronomy, Institute for Space Imaging Science, University of Lethbridge, Lethbridge AB T1K 3M4, Canada*
[7]*Royal Observatory of Belgium, Ringlaan 3, B-1180 Brussels, Belgium*

Accepted 2013 October 4. Received 2013 October 4; in original form 2013 July 24

ABSTRACT

We present an analysis of the far-infrared and submillimetre molecular emission-line spectrum of the luminous M-supergiant VY CMa, observed with the Spectral and Photometric Imaging Receiver (SPIRE) and Photodetector Array Camera and Spectrometer for *Herschel* spectrometers aboard the *Herschel Space Observatory*. Over 260 emission lines were detected in the 190–650 μm SPIRE Fourier Transform Spectrometer spectra, with one-third of the observed lines being attributable to H_2O. Other detected species include CO, ^{13}CO, $H_2^{18}O$, SiO, HCN, SO, SO_2, CS, H_2S and NH_3. Our model fits to the observed ^{12}CO and ^{13}CO line intensities yield a $^{12}C/^{13}C$ ratio of 5.6 ± 1.8, consistent with measurements of this ratio for other M-supergiants, but significantly lower than previously estimated for VY CMa from observations of lower-*J* lines. The spectral line energy distribution for 20 SiO rotational lines shows two temperature components: a hot component at ∼1000 K, which we attribute to the stellar atmosphere and inner wind, plus a cooler ∼200 K component, which we attribute to an origin in the outer circumstellar envelope. We fit the line fluxes of ^{12}CO, ^{13}CO, H_2O and SiO, using the SMMOL non-local thermodynamic equilibrium (LTE) line transfer code, with a mass-loss rate of $1.85 \times 10^{-4}\,M_\odot\,yr^{-1}$ between $9R_*$ and $350R_*$. We also fit the observed line fluxes of ^{12}CO, ^{13}CO, H_2O and SiO with SMMOL non-LTE line radiative transfer code, along with a mass-loss rate of $1.85 \times 10^{-4}\,M_\odot\,yr^{-1}$. To fit the high rotational lines of CO and H_2O, the model required a rather flat temperature distribution inside the dust condensation radius, attributed to the high H_2O opacity. Beyond the dust condensation radius the gas temperature is fitted best by an $r^{-0.5}$ radial dependence, consistent with the coolant lines becoming optically thin. Our H_2O emission-line fits are consistent with an ortho:para ratio of 3 in the outflow.

Key words: radiative transfer – stars: individual: VY CMa – stars: mass-loss – ISM: molecules – infrared: stars – submillimetre: stars.

1 INTRODUCTION

VY Canis Majoris is a high-luminosity M-supergiant (2–$3 \times 10^5\,L_\odot$ for the parallax distance of 1.14 ± 0.09 kpc; Choi et al. 2008) with a very high mass-loss rate (∼$2 \times 10^{-4}\,M_\odot\,yr^{-1}$; Danchi et al. 1994; De Beck et al. 2010). It is self-obscured by its dusty circumstellar envelope, which has produced a reflection nebula at optical wavelengths (Humphreys, Helton & Jones 2007). Due

Herschel is an ESA space observatory with science instruments provided by European-led Principal Investigator consortia and with important participation from NASA.

† E-mail: mikako@star.ucl.ac.uk

to its brightness and high mass-loss rate, VY CMa has been studied extensively from optical to millimetre wavelengths (e.g. Monnier et al. 1999). Its far-infrared spectrum shows numerous water lines (Neufeld et al. 1999; Polehampton et al. 2010), while several water maser lines have been discovered at submillimetre wavelengths (e.g. Menten et al. 2006). In addition to CO, SiO, H_2O and other oxygen-rich molecules, carbon-rich species, such as HCN and CS, have also been found in the spectrum of this oxygen-rich object (Ziurys et al. 2007).

The far-infrared and submillimetre spectra of red supergiants and asymptotic giant branch (AGB) stars exhibit numerous molecular emission lines (e.g. Barlow et al. 1996; Royer et al. 2010). These can be used to investigate the physical and chemical state of the circumstellar material, with different transitions probing specific density and temperature domains. Water vapour rotational emission lines are particularly strong in the far-infrared and submillimetre spectra of cool oxygen-rich stars and can be important coolants of their stellar wind outflows (e.g. Deguchi & Nguyen-Q-Rieu 1990; Kaufman & Neufeld 1996). Following the publication of our initial *Herschel* spectroscopic results for VY CMa (Royer et al. 2010), we present here a more detailed analysis of our Spectral and Photometric Imaging Receiver (SPIRE) and Photodetector Array Camera and Spectrometer (PACS) spectra of several molecular species, in particular non-local thermodynamic equilibrium (non-LTE) radiative line transfer models for observed CO, SiO and H_2O transitions. This modelling has enabled us to find best-fitting radial temperature and density profiles for VY CMa's outflow, as well as allowing an estimate to be made of its $^{12}C/^{13}C$ isotopic ratio.

2 OBSERVATIONS AND LINE IDENTIFICATIONS

The *Herschel Space Observatory* (hereafter *Herschel*) was launched in 2009 May (Pilbratt et al. 2010) with three instruments on board: SPIRE (Griffin et al. 2010), PACS (Poglitsch et al. 2010) and HIFI (de Graauw et al. 2010). We report here observations made with the SPIRE Fourier Transform Spectrometer (FTS) and with the PACS grating spectrometer, which together cover the wavelength range from 55 to 650 μm. The SPIRE FTS covers the 190–650 μm wavelength range, simultaneously, while the PACS spectrometer covers the 55–210 μm spectral range, similar to that covered by the Long Wavelength Spectrometer (LWS) on board the *Infrared Space Observatory* (*ISO*; Clegg et al. 1996), although with higher spectral resolution and greater sensitivity.

Fig. 1 shows the observed spectral energy distribution (SED) of VY CMa, including spectrophotometry from the *ISO* Short Wavelength Spectrometer (SWS) and LWS instruments (black) and the *Herschel* PACS (red) and SPIRE (blue) spectrometers.

2.1 SPIRE FTS spectra

The SPIRE FTS simultaneously covers the SLW short wavelength band (190–313 μm; 31–52 cm^{-1}; 957–1577 GHz) and SLW long wavelength band (303–650 μm; 15–33 cm^{-1}; 461–989 GHz). VY CMa was observed with the SPIRE FTS as part of the MESS (Mass-loss of Evolved StarS) Guaranteed Time Key Programme (Groenewegen et al. 2011), first during *Herschel*'s performance verification phase and again during nominal operations. The first SPIRE FTS spectrum was obtained on 2009 September 13 (OD 123, obsid 1342183813). The on-source integration time was 3996 s, corresponding to 60 FTS scans. The second FTS spectrum was obtained on 2010 March 27 (OD 317, obsid 1342192834) with an on-source integration time of 2264 s, corresponding to 34 FTS scans.

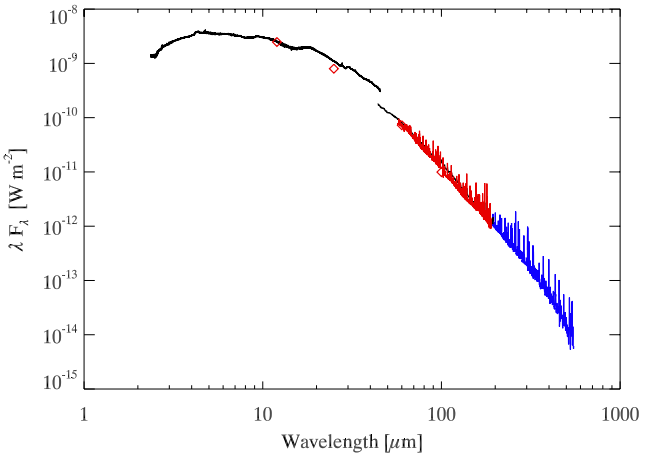

Figure 1. The infrared SED of VY CMa. The SPIRE FTS spectrum covers the 194–670 μm range (blue), while the PACS spectrum covers the 55–190 μm range (red). Additional data points include the *ISO* SWS spectrum (Sloan et al. 2003) and the *ISO* LWS spectrum (Polehampton et al. 2010), both shown in black, and the *IRAS* point source catalogue fluxes (Beichman et al. 1988), shown as red diamonds. Numerous emission lines are visible in the PACS and SPIRE spectra.

We reduced the spectra with the first reliable version of the *Herschel* Interactive Processing Environment software (version 4 of HIPE; Fulton et al. 2008) using the standard point source pipeline described by Fulton et al. (2010) and the calibration scheme described by Swinyard et al. (2010). Since the initial data reduction, an improved pipeline and calibration scheme has been evolved (HIPE v11, Fulton et al., in preparation), which provides much superior calibration and noise reduction for faint sources. VY CMa is a bright source for the SPIRE FTS and we find that comparison of the latest reduction with the reduction used in this paper shows no discernible difference in flux or noise levels. The SPIRE FTS calibration is now based on the spectrum of Uranus and detailed analysis of the flux uncertainties (Swinyard et al., in preparation) shows that the absolute flux on a source of this brightness is absolutely calibrated to within 6 per cent.

FTS produce spectra in which lines have sin c profile functions. To mitigate the effects on weak lines of negative side-lobes from many bright lines, we apodized the interferograms using the extended Norton–Beer function 1.5 (Naylor & Tahic 2007). This yielded spectra in which the line profiles, which were close to Gaussian, had a full width at half-maximum (FWHM) of 0.072 cm^{-1}, compared to the unapodized spectral resolution of 0.048 cm^{-1}. Since FTS produce spectra that are linearly sampled in frequency, all our FTS spectral measurements have been made in frequency space.

2.2 PACS CO line spectra

VY CMa was observed with the PACS spectrometer on 2009 November 3 (OD 173) using the full-range SED mode with a single repetition. The observations were taken in 'chop-nodded' mode, each with a single nodding cycle, and using the smallest chopper throw available (1 arcmin). The total duration of the observations was 3655 s for the 54–73 μm and 102–210 μm ranges, and 2759 s for the 67–109.5 μm and 134–219 μm ranges. The data from the central spaxel were extracted and reduced with version 10 of HIPE (Ott 2010) and calibration set 45. With this set, the absolute flux calibration is based on comparisons of PACS' internal calibration sources with celestial standards on the central nine spaxels of the

instrument. The calibration is established at one key wavelength per camera and per band, and transferred to the other wavelengths via a relative spectral response function calibrated on the ground. After extraction and before 'beam correction', a simple pointing correction was applied to the flux in the central spaxel, by scaling it so that its continuum matched the one measured in the integral of the central 3×3 spaxels. This correction is part of the absolute flux calibration scheme as it brings our spectrum to the same reference as used to establish the absolute flux calibration files (i.e. the nine central spaxels). In our case, it is of the order of 15 per cent in all bands, and corrects for flux missing from the central spaxel due to e.g. a slight mispointing, or pointing jitter and/or marginal source extension. Additional details of the PACS observations and data reduction are provided by Royer et al. (2010). The absolute flux calibration accuracy is estimated to be 20 per cent (Poglitsch et al. 2010). For eight ^{12}CO lines in the spectrum that had sufficiently good signal-to-noise ratios, Gaussian fits yielded the integrated line fluxes that are listed in Table A1 of Appendix A (the PACS spectrum contains more than 400 molecular emission lines, an overview of which is presented by Royer et al. 2010).

2.3 SPIRE line fluxes and identifications

Prior to line identification and analysis, we measured the emission-line fluxes in continuum-subtracted versions of the SPIRE FTS spectra. The continuum fits were obtained by fitting spline curves to connect user-identified points that were judged to correspond to local continuum levels through the spectra. Fig. 2 shows the

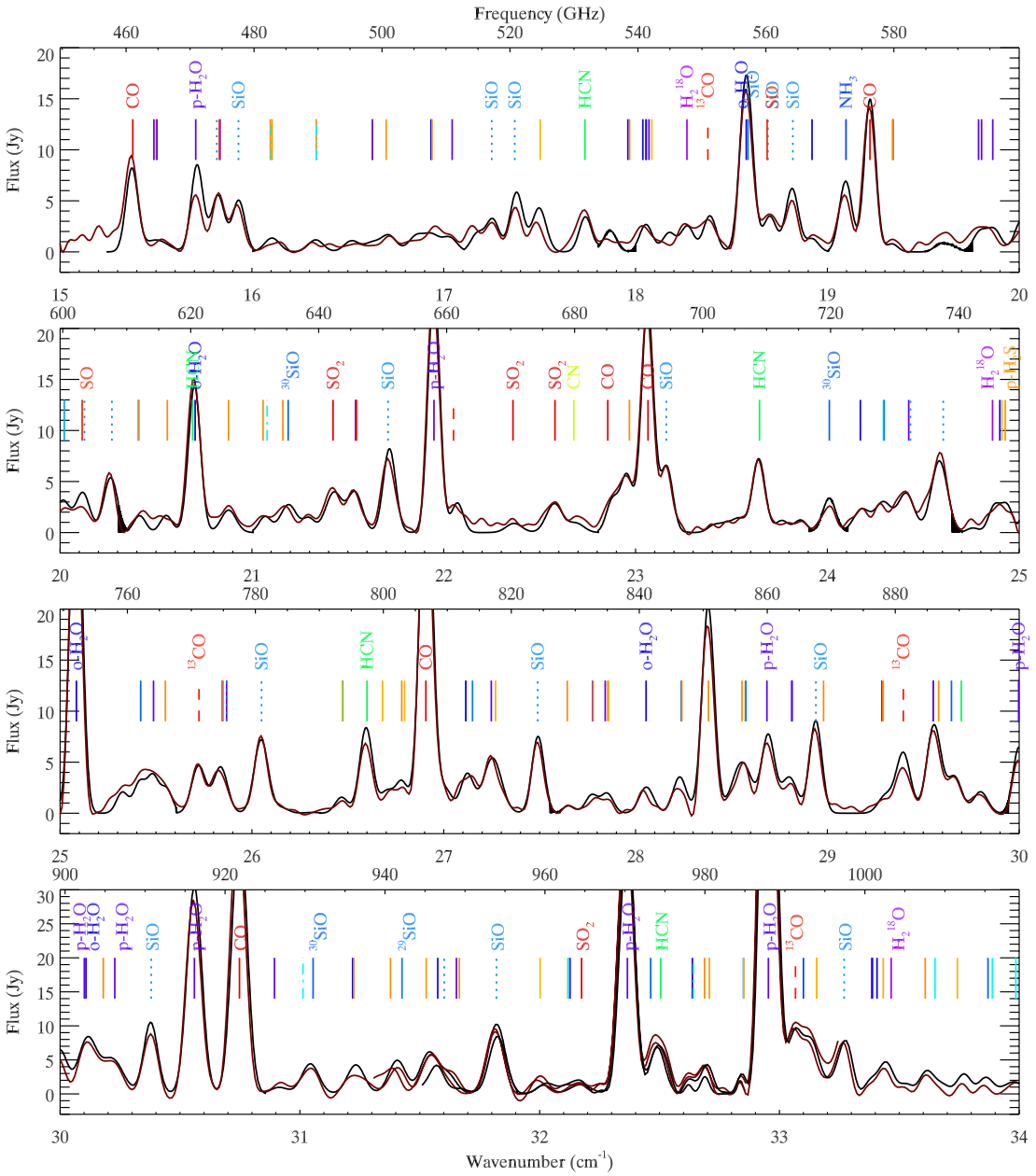

Figure 2. The SPIRE FTS spectrum of VY CMa after continuum-subtraction. The black line shows the OD 123 spectrum and the brown line shows the OD 317 spectrum. Representative molecular identifications are labelled with different colour and line styles; occasionally vertical lines overlap. A full list of molecular line identifications can be found in Tables A2 and A3. The region between 31 and 33 cm^{-1} was covered by both the SLW and SSW subspectra.

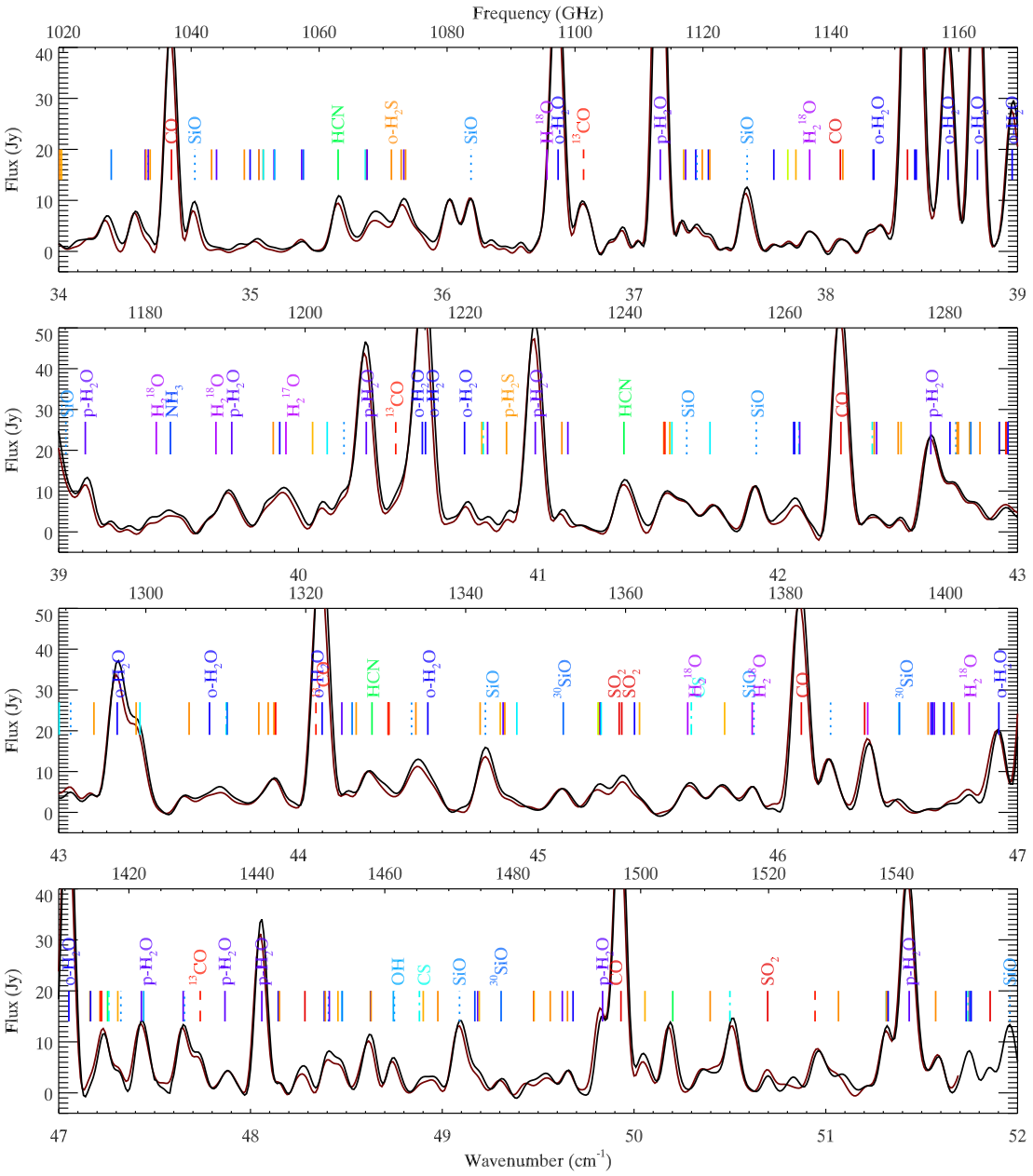

Figure 2 – *continued*

continuum-subtracted SPIRE FTS spectra corresponding to the two different observation dates (OD 123 and 317). The two spectra are almost identical, although there are slight differences in the shapes of weak features at the lowest frequencies (<20 cm^{-1} = 600 GHz). This is because the continuum fluxes at these frequencies fall to levels where the flux uncertainties are larger than over the rest of the spectrum. The spectral range 939–999 GHz was covered by both the SSW and SLW subspectra.

The emission lines in the apodized SPIRE FTS spectra were fitted by Gaussian profiles using the emission line fitting (ELF) suite of programs written by P. J. Storey that are part of the DIPSO spectral analysis package mainly written by I. D. Howarth. The continuum-subtracted spectra were divided into smaller subspectra, for which about 20 emission lines at a time were fitted simultaneously with ELF. Since the lines were unresolved, all the lines in each sub-spectrum were required to have the same FWHM. Over 260 emission lines were measured in total.

Amongst oxygen-rich AGB stars and red supergiants, VY CMa is one of the best studied at millimetre wavelengths (e.g. Tenenbaum et al. 2010). Detected molecules include CS, HCN, HNC, CN, H_2S, NH_3, SiS, SO, SO_2, TiO, TiO_2 (Ziurys et al. 2007, 2009; Kaminski et al. 2013), in addition to molecules commonly found in the spectra of oxygen-rich AGB stars, such as CO, H_2O, OH and SiO.

Since most of the emission lines in the SPIRE FTS spectra are expected to be molecular transitions, we mainly searched molecular data bases (e.g. Pickett 1991; Müller et al. 2005). Since there were multiple candidate transitions per observed line, in order to eliminate unlikely identifications we calculated molecular spectra based on an LTE radiative emission code (Matsuura et al. 2002), for species where Einstein coefficients or line intensities were

available (Sauval & Tatum 1984; Langhoff & Bauschlicher 1993; Müller et al. 2005; Rothman et al. 2009), namely CO, CN, CS, H_2O, H_2S, HCN, HCO^+, HNC, H^3O^+, OH, NH_3, SiO, SiS, SO, SO_2 and their isotopes, and compared the predicted line intensity patterns with the measured spectrum.

Tables A2 and A3 list for the detected lines in the SPIRE FTS spectra the measured line centre wavenumbers, integrated fluxes and the statistical uncertainties in these quantities as estimated by ELF, along with the rest frequencies (in cm^{-1} and GHz) and wavelengths (in μm) of the proposed line identifications. These identifications are also indicated in Fig. 2. Multiple identifications corresponding to more than three transitions are not plotted, but are indicated by vertical bars. The sources for the rest frequencies were the HITRAN data base (Rothman et al. 2009) for CO, ^{13}CO, H_2O, $H_2^{18}O$, OH, SO_2, HCN, CS, NH_3 and H_2S, the JPL line data base (Pickett et al. 1998) for HNC, SO, HCO^+, CN and H_3O^+ and the CDMS data base (Müller et al. 2005) for SiO. Our list of SPIRE FTS line identifications for the oxygen-rich outflow from VY CMa complements those for three carbon-rich evolved sources that were presented by Wesson et al. (2010).

Of the more than 260 lines in VY CMa's 460–1580 GHz spectral region, listed in Tables A2 and A3, nearly one-third are attributed to H_2O, with the strongest lines in the spectrum being pure rotational (ν_1, ν_2, $\nu_3 = 0$) transitions of water. Vibrationally excited H_2O rotational lines, in particular $\nu_2 = 1$ transitions, are also clearly detected. The pure rotational ($v = 0$) lines of ^{12}CO, ^{13}CO and HCN are strong and SiO rotational transitions also tend to be strong at longer wavelengths. SO and SO_2 contribute weaker lines; these molecules have numerous transitions in this wavelength range and could potentially contribute many unresolved lines. Due to line blending, many weak lines still do not have firm identifications.

Justtanont et al. (2012) reported the detection of five SiO lines in the *Herschel* HIFI spectra of nine oxygen-rich AGB stars. These included pure rotational lines of SiO at 607.599 GHz (20.26 cm^{-1}; $J = 14$–13) and 694.275 GHz (23.16 cm^{-1}; $J = 16$–15), along with vibrationally excited ($v = 1$) SiO rotational lines at 560.326 GHz (18.69 cm^{-1}; $J = 13$–12), 646.429 GHz (21.56 cm^{-1}; $J = 15$–14) and 990.355 GHz (33.03 cm^{-1}; $J = 23$–22). These transitions and more are detected in the VY CMa SPIRE spectra. Ground-based Atacama Pathfinder Experiment (APEX) observations have detected ^{29}SiO and ^{30}SiO pure rotational lines in the submillimetre spectra of VY CMa (Menten et al. 2006). Transitions from these species are also detected in the SPIRE FTS spectra.

Menten et al. (2010) reported the detection of the 1_0–0_0 transition of ortho-NH_3 at 572.4981 GHz (19.096 cm^{-1}) from VY CMa. This transition was detected as a relatively strong line in the SPIRE spectra. Other NH_3 lines are not obvious.

A number of far-infrared and submillimetre H_2O lines have been predicted to mase (Deguchi & Nguyen-Q-Rieu 1990; Neufeld & Melnick 1991; Yates, Field & Gray 1997). For VY CMa, Harwit et al. (2010) reported the H_2O 5_{32}–4_{41} transition at 620.70 GHz (20.70 cm^{-1}) to be masing, while Menten et al. (2008) found the H_2O 6_{42}–5_{51} transition at 470.889 GHz (15.70 cm^{-1}) and the 5_{33}–4_{40} transition at 474.680 GHz (15.83 cm^{-1}) to be masing. Menten & Young (1995) reported the 1_{10}–1_{01} $\nu_2 = 1$ transition at 658.01 GHz (21.95 cm^{-1}) to be masing. These lines were all detected in the SPIRE FTS spectra. However, their line fluxes are not particularly strong compared to those of other H_2O lines, suggesting that line strength alone may be an insufficient criterion to distinguish a maser line from a thermally excited line – we return to this question in Section 4.4.

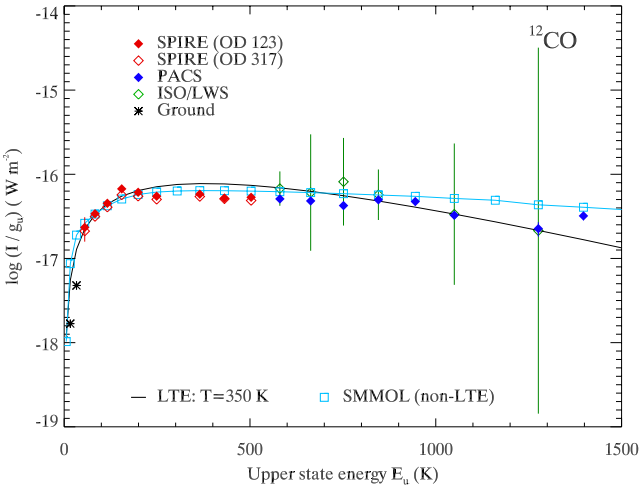

Figure 3. The spectral line energy distribution for VY CMa's pure rotational ^{12}CO transitions. Together with SPIRE and PACS spectrometer measurements, we have included *ISO*/LWS line flux data (Polehampton et al. 2010) and the JCMT $J = 2$–1 and 3–2 measurements of Kemper et al. (2003). The large error bars pertain to the *ISO*/LWS line flux measurements; those for the *Herschel* PACS and SPIRE line fluxes are smaller than the symbol sizes. We have also plotted model CO line intensities from an LTE model (solid line) and from the SMMOL NLTE model described in Section 4 (open squares).

3 LTE EMISSION-LINE ANALYSIS

In the case of optically thin LTE emission, a spectral line energy distribution (e.g. Fig. 3) can provide an estimate of the excitation temperature and the number of emitting molecules, with the upper level energy E_u at the peak of the overall curve providing an estimate of the excitation temperature (T_{ex}) of the molecules (Goldsmith & Langer 1999). We adopted molecular constants from the HITRAN data base (Rothman et al. 2009), except for SiO, where we adopted A-coefficients from Langhoff & Bauschlicher (1993) and wavenumbers from Müller et al. (2005). Theoretical line intensities were then calculated using an LTE radiative transfer code (Matsuura et al. 2002). The resultant fits are summarized in Table 1.

Justtanont et al. (2000) and Polehampton et al. (2010) used *ISO*/LWS measurements to estimate excitation temperatures for CO. We note that a single-line trend is found only for some simple diatomic and linear triatomic molecules. Water, for example, has three rotational dipole moments, so its Einstein A-coefficients are more complicated and its modified rotational diagram does not follow *a single-curve* relation (Goldsmith & Langer 1999). For CO, SiO and HCN, we present our results in the form of observed and model spectral line energy distributions, whereas for H_2O, we compare observed with non-LTE (NLTE) model line spectra in Section 4.

Table 1. Results from LTE fits to the spectral line energy distributions.

Molecule	T_{ex} (K)	No. of molecules	Mass ($M_\odot$)
CO	350 ± 90	$(1.2 \pm 0.4) \times 10^{52}$	$(2.9 \pm 0.7) \times 10^{-4}$
^{13}CO	350 ± 90	$(1.8 \pm 0.9) \times 10^{51}$	$(4.8 \pm 2.5) \times 10^{-5}$
SiO (hot)	∼1000	4×10^{48}	2×10^{-7}
SiO (cold)	200	2×10^{48}	7×10^{-8}
HCN	250 ± 50	$(2.7 \pm 2.1) \times 10^{48}$	$(6.6 \pm 0.5) \times 10^{-8}$

3.1 The ^{12}CO lines

Fig. 3 shows the ^{12}CO spectral line energy distribution for VY CMa. The plotted line fluxes are from the SPIRE and PACS spectra, along with the *ISO*/LWS line flux measurements of Polehampton et al. (2010). We have plotted the SPIRE line measurements from both epochs. We have also included ground-based CO $J = 2$–1 and 3–2 line flux measurements made with the James Clerk Maxwell Telescope (JCMT; Kemper et al. 2003). The ground-based observations of these two lines by Ziurys et al. (2009) gave line fluxes that are consistent with those of Kemper et al. (2003).

The measured SPIRE, PACS and *ISO*/LWS ^{12}CO line fluxes approximately follow an LTE distribution that can be fitted with an excitation temperature of 350 ± 90 K, see Fig. 3. Polehampton et al. (2010) estimated a ^{12}CO excitation temperature of 250 ± 140 K, consistent with our value within the respective uncertainties. We also modelled the ^{12}CO line intensities using the NLTE code SMMOL; details of the models are given in Section 4.

Ground-based measurements of several ^{12}CO lines in the *Herschel* range are available for VY CMa. Kemper et al. (2003) reported a CO $J = 6$–5 line flux of 1.4×10^{-16} W m^{-2}. They also observed the CO $J = 7$–6 line, with a line flux of 2.2×10^{-16} W m^{-2}. These fluxes are a factor of 4–5 times smaller than our SPIRE FTS measurements in Table A2. Kemper et al. used the JCMT for which the half-power beamwidth for the 6–5 and 7–6 lines was 8 and 6 arcsec, respectively. Muller et al. (2007) reported the angular diameter of VY CMa to be almost 10 arcsec in the CO $J = 2$–1 line, so it is possible that the JCMT observations of the higher-J CO lines resolved out some of their emission. The SPIRE FTS beam has an FWHM of ∼37 arcsec in the 303–650 μm (15–33 cm^{-1}; 461–989 GHz) SLW region and ∼18 arcsec in the 190–313 μm (31–52 cm^{-1}; 957–1577 GHz) SSW region (Swinyard et al. 2010), significantly larger than that of the JCMT.

3.2 The ^{13}CO lines and the ^{12}C/^{13}C ratio

The ^{12}C/^{13}C isotope ratio can be estimated from observations of the lines of ^{12}CO and ^{13}CO. We measured a mean ^{12}CO/^{13}CO line flux ratio of 7.0 ± 1.8 in the OD123 and in the OD317 SPIRE FTS spectra (eight matched pairs of transitions in each spectrum, from 5–4 to 13–12, with the blended 12–11 transition omitted). If the transitions are all optically thin, then this ratio should be close to the ^{12}C/^{13}C ratio. Our LTE fits to the ^{12}CO and ^{13}CO spectral line energy distributions (Figs 3 and 4) yielded an excitation temperature of 350 ± 90 K and a ^{12}C/^{13}C ratio of 6.2 ± 2.0. Finally, our best-fitting NLTE model for ^{12}CO and ^{13}CO (Table 2) implies a ^{12}C/^{13}C ratio of 5.6 ± 1.8 for VY CMa.

Our ^{12}C/^{13}C isotopic ratio of 5.6 ± 1.8 is significantly lower than previously reported values for VY CMa, but is within the range of the ^{12}C/^{13}C ratios of 3–14 measured for four other red supergiants by Milam, Woolf & Ziurys (2009), who derived a ^{12}CO/^{13}CO ratio of 25–46 for VY CMa using the $J = 1$–0 and 2–1 ^{12}CO and ^{13}CO lines. Nercessian et al. (1989) estimated a ^{12}C/^{13}C ratio of 36 ± 9, using the $J = 1$–0 HCN and H^{13}CN lines. Our NLTE models for ^{12}CO and ^{13}CO imply that their lowest transitions are optically thick, while the ^{12}CO $J = 5$–4 and higher transitions are optically thin. It is noticeable in the plots of De Beck et al. (2010) that while the profiles of the CO 2–1 and 3–2 transitions show several pronounced peaks and troughs, the 4–3, 6–5 and 7–6 transitions show increasingly Gaussian-like line profiles; De Beck et al. (2010) derived a ^{12}C/^{13}C ratio of 14.8, much closer to the ratio derived from the 4–3 to 13–12 lines in the SPIRE-FTS spectra than those obtained by observers making use of lower-J lines. We believe that our ^{12}C/^{13}C ratio of 5.6 ± 1.8 for VY CMa is reliable and removes an anomaly by yielding an isotopic ratio that is consistent with those found for other red supergiants.

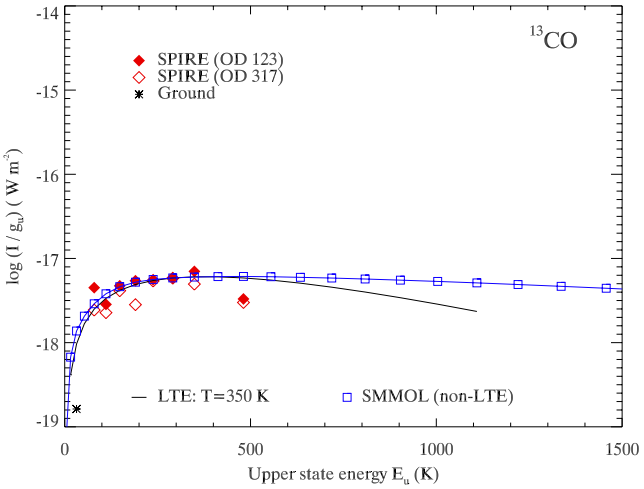

Figure 4. The spectral line energy distribution for the pure rotational transitions of ^{13}CO measured in the SPIRE FTS spectra of VY CMa.

3.3 HCN

Emission lines from the carbon-bearing molecule HCN are predominantly found in the spectra of carbon-rich AGB stars but have also been found in the spectra of several oxygen-rich AGB stars at millimetre wavelengths (e.g. Deguchi & Goldsmith 1985; Nercessian et al. 1989). HCN emission was detected from the F8 supergiant IRC+10420 by Jewell, Snyder & Schenewerk (1986), while Ziurys et al. (2009) detected HCN, HNC, CN and CS emission from VY CMa. Over 10 HCN lines have been detected in our *Herschel* FTS spectra of VY CMa, where this molecule is responsible for lines of intermediate strength. Fig. 5 shows the spectral line energy distribution for HCN obtained from the SPIRE FTS data. It has been fitted with an LTE model having $T_{ex} = 250 \pm 50$ K, lower than that derived for CO, which could indicate that HCN originates from cooler outer parts of the circumstellar envelope.

Nercessian et al. (1989), Charnley, Tielens & Kress (1995) and Willacy & Millar (1997) have investigated processes which can trigger the formation of carbon-bearing molecules in oxygen-rich circumstellar envelope. Charnley et al. (1995) and Willacy & Millar (1997) used CH_4 as a parent molecule and formed carbon-bearing molecules through photochemical processes mediated by the interstellar UV radiation field. Their models predicted a peak fractional abundance of HCN at about 10^{16}–10^{17} cm in radius. This is in contrast with CO, which was predicted to have an almost constant abundance from 10^{15} cm out to 10^{18} cm. Their models were for AGB stars, so for red supergiants, the overall sizes would have to be scaled up. The predicted lack of HCN in the inner part of the outflow could be responsible for the lower HCN excitation temperature compared to that of CO. In contrast, Duari, Cherchneff & Willacy (1999) investigated shock chemistry in the extended atmosphere, i.e. just above the photosphere. This can also form carbon-bearing molecules in oxygen-rich environments and they favoured shock chemistry to account for the HCN observed around IK Tau. Shock formation of HCN in the innermost parts of an outflow, where CO also exists, would be expected to lead to similar HCN and CO

Table 2. Parameters of the NLTE model that produced the best fits to the *Herschel* ^{12}CO, ^{13}CO, SiO and H_2O line fluxes of VY CMa.

Model parameters		^{12}CO	^{13}CO	H_2O	SiO
Stellar radius R_* (cm)	1.44×10^{14}				
$R_{\rm inner}$: inner radius of molecular gas envelope (cm)	1.44×10^{14}				
$R_{\rm inner,dust}$: inner radius of dust envelope (cm)	1.283×10^{15}				
$R_{\rm outflow,break}$: radius of density discontinuity (cm)	5.0×10^{16}				
$R_{\rm outer,dust}$: outer radius of model (cm)	2.93×10^{17}				
β: density law index[a]	2.0				
α: Kinetic temperature law index[a]	0.6				
Turbulent velocity (km s^{-1})	1.0				
X: fraction of molecule/H_2		2.5×10^{-4}	4.5×10^{-5}	2×10^{-4}	8×10^{-5}
Dust optical depth in the V band	50				
$\rho_{\rm d}$: density of dust (g cm^{-3})	3.0				
Gas-to-dust mass ratio: $\rho_{\rm g}/\rho_{\rm d}$	267				
Wind velocities: v_∞ and $v_{\rm inner}$ (km s^{-1})	44.0, 4.0				
Inner radius of velocity law (cm)	1.283×10^{15}				
γ: velocity law index[a]	0.2				
Stellar temperature (K)	2800				
Sublimation temp. of molecule (K)		20	20	100	(1000)/100
Mass-loss rate between $R_{\rm inner,dust}$ and $R_{\rm outflow,break}$ ($M_\odot$ yr^{-1})	1.85×10^{-4}				
Mass-loss rate beyond $R_{\rm outflow,break}$ ($M_\odot$ yr^{-1})	9.3×10^{-5}				
Dust emissivity behaviour $\kappa(>250\ \mu$m)	λ^{-1}				
H_2O ortho:para ratio				3:1	
$R_{T,\rm break}$: Radius of break in temperature (cm)	5×10^{14}				
New kinetic temperature law index α at $R_{T,\rm break}$	0.15				
SiO density reduction factor at $R_{\rm inner,dust}$[b]					20

[a]Gas temperature, density and velocity laws used for the NLTE line modelling: Temperature: $(r/R_{\rm inner})^{-\alpha}$, Gas density: $(r/R_{\rm inner})^{-\beta}$, Velocity: $v(r) = v_{\rm inner} + (v_\infty - v_{\rm inner})(1 - R_{\rm inner,\,dust}/r)^\gamma$, for $r \geq R_{\rm inner,\,dust}$.
[b]The SiO density reduced by a factor 20 at $R_{\rm inner,\,dust}$, attributed to dust condensation, with residual SiO extending out to a radius corresponding to a gas temperature of 20 K.

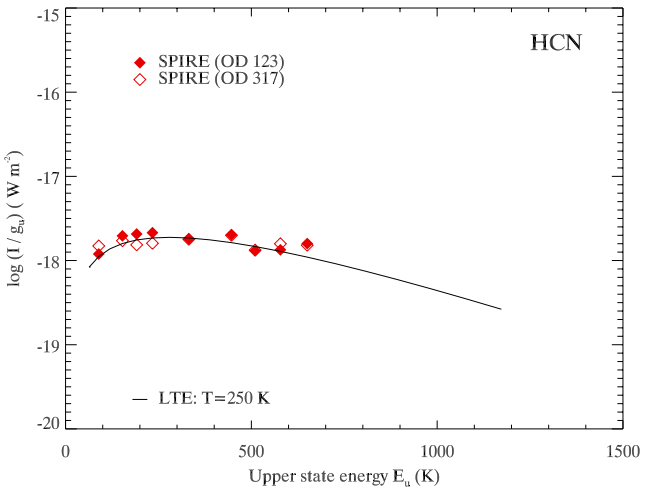

Figure 5. The spectral line energy distribution for the pure rotational transitions of HCN measured in the SPIRE FTS spectra of VY CMa.

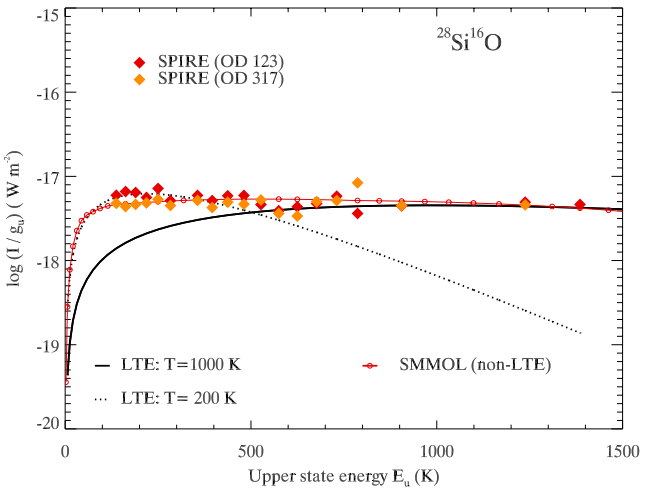

Figure 6. The spectral line energy distribution of the pure rotational transitions of SiO measured in the SPIRE FTS spectra of VY CMa.

spectral line energy distributions, or to even give HCN a higher excitation temperature than CO. This is not in agreement with our SPIRE FTS observations of CO (Fig. 3) and HCN (Fig. 5), so for HCN this appears to favour an origin in the cooler outer parts of the outflow, i.e. via photochemical processes mediated by the interstellar radiation field.

3.4 SiO

More than 20 SiO lines were detected in the SPIRE spectra. The spectral line energy distribution for the pure rotational transitions in $v = 0$ of SiO shows a double peak (Fig. 6): the first peak is at about $E_{\rm u} \sim$ 100–200 K, with the line intensities dipping until about $E_{\rm u} \sim 500$ K and then rising again for $E_{\rm u} > 500$ K. The fits to these lines suggest a cool component with $T_{\rm ex} = 200$ K and a hotter component with $T_{\rm ex} \sim 1000$ K. The latter value is rather uncertain, because its peak $E_{\rm u}$ is not well constrained.

These two SiO components could reflect the chemistry and structure of VY CMa's outflow. Signatures of deep regions of its atmosphere have been found in its near- and mid-infrared molecular emission (e.g. Tsuji et al. 1997). The excitation temperature of molecular gas associated with the extended atmosphere and inner

envelope is typically 500–1500 K (e.g. Tsuji et al. 1997; Ireland, Scholz & Wood 2011), similar to the excitation temperature found here for the hotter SiO component (∼1000 K), so it appears likely that the hot SiO component is associated with gas in the inner outflow. Further out in the extended envelope dust forms, and radiation pressure on dust grains can drive the outflow, creating the circumstellar envelope from which the cooler SiO component originates.

4 NLTE MODEL ANALYSIS

The far-IR and submillimetre spectra of VY CMa display a host of molecular emission lines, many of which are due to water vapour. Some of these molecular lines may have significant optical depths and are most likely not in LTE, so that NLTE radiative transfer codes are required to interpret the physical conditions in the line emitting regions. We have modelled the *Herschel* spectra of VY CMa using the NLTE code SMMOL (Rawlings & Yates 2001).

4.1 Basic parameters

VY CMa has been studied extensively and its basic parameters are well constrained. The parallax measurements by Choi et al. (2008) obtained a distance of 1.14 ± 0.09 kpc, and we have used this distance here. The effective temperature is adopted to be 2800 K (Sidaner & Le Bertre 1996) and we adopt a stellar radius of $R_* = 2069\,\mathrm{R}_\odot$, corresponding to a luminosity of $2.37 \times 10^5\,\mathrm{L}_\odot$. Table 2 lists the main parameters used for our SMMOL wind models.

The first task was to construct a dust radiative transfer model to fit the observed SED in order to estimate the dust grain properties: the inner dust condensation radius, the radial density and temperature distributions of the dust grains. This was calculated with a one-dimensional and spherically symmetric model using the DART dust radiative transfer code of Efstathiou & Rowan-Robinson (1990), whose result was also compared with Monte Carlo radiative transfer code (Ercolano, Barlow & Storey 2005). The dust was assumed to consist of astronomical silicates (Draine & Lee 1984) with an MRN (Mathis, Rumpl and Nordsieck) size distribution of the form $n(a)\,\mathrm{d}a \propto a^{-3.5}\mathrm{d}a$, for grains with radii a between 0.005 and 0.25 μm (Mathis, Rumpl & Nordsieck 1977). Although the MRN distribution was derived for interstellar grains, similar power-law distributions are expected wherever grain–grain collisions determine their size distributions, including stellar outflows (Biermann & Harwit 1980). A best fit was found to the SED of VY CMa and the resulting dust temperature radial profile was used as an initial input into the line radiative transfer calculations. The fit required a dust condensation inner radius of $9R_*$ and an outer radius of at least $830R_*$.

The mass-loss structure and history of VY CMa has been discussed by Decin et al. (2006) and by Muller et al. (2007). Decin et al. used a spherically symmetric wind model with line radiative transfer to interpret the ground-based CO spectra and deduced that it had undergone a phase of high mass-loss ($\sim 3.2 \times 10^{-4}\,\mathrm{M}_\odot\,\mathrm{yr}^{-1}$) some 1000 yr ago and lasting for some 100 yr, preceded by a lower mass-loss rate phase lasting some 800 yr. Muller et al. deduced that the inner part of VY CMa's envelope has been undergoing a phase of enhanced mass-loss that began about 100 yr ago. Our adopted terminal velocity of $44\,\mathrm{km\,s}^{-1}$ for the outflow is based on half the full widths at zero intensity of CO line profiles presented by Kemper et al. (2003), as well as on expansion velocities determined by Richards, Yates & Cohen (1998) and Menten et al. (2008) from H_2O masers.

4.2 NLTE line radiative transfer calculations

The molecular line radiative transfer and level population code SMMOL (Rawlings & Yates 2001) uses the accelerated lambda iteration (ALI) scheme described by Scharmer & Carlsson (1985) and Rybicki & Hummer (1991) to solve the coupled level population and line radiative transfer problem exactly and quickly. These methods, designed to solve line radiative transport in optically thick stellar atmospheres, are ideal for solving the radiative transport by water molecules in the outflows from AGB stars and red supergiants. In these outflows, it is clear that many ground vibrational state transitions of water and CO are optically thick at their line centres and ALI methods are needed to achieve an exact converged solution for the level populations and radiation field.

SMMOL uses a fine grid in position–velocity space to allow the inclusion of the effects of maser emission in the calculation of level populations. This is particularly important for an outflow such as that of VY CMa, which has very bright H_2O maser emission lines at submillimetre wavelengths (Menten et al. 2008; Harwit et al. 2010), which can saturate and affect level populations. In a paper on Orion-KL H_2O line emission (Lerate et al. 2010), we used approximate $H_2{}^{16}O$–H_2 collisional parameters based on H_2O–He cross-sections (Green, Maluendes & McLean 1993). Here, we use $H_2^{16}O$–H_2 cross-sections calculated by Faure & Josselin (2008) along with water vapour molecular data from the H_2O line list (containing half a billion lines) produced by Barber et al. (2006). The data include the 45 lowest rotational energy levels in the ground vibrational states of both ortho- and para-H_2O, colliding with both para- and ortho-H_2, covering a kinetic temperature range of 20–2000 K.

For ^{12}CO and ^{13}CO, we use the CO–H_2 cross-sections calculated by Yang et al. (2010) with molecular data from Müller et al. (2005). This provided CO energy level and collisional data up to $J = 40$, for kinetic temperatures ranging from 2 to 3000 K. These collisional rates were for collisions with both para- and ortho-H_2.

The SiO–H_2 collisional excitation rates were based on the SiO–He calculations of Dayou & Balança (2006), scaled by a factor of 1.38 in order to account for the difference between the He and H_2 cross-sectional areas. The calculations included 41 rotational transitions only, ignoring vibrationally excited transitions, which could potentially cause errors for molecular lines arising from high-temperature gas, typically over 1000 K. These errors could particularly influence line intensities from SiO molecules located inside the dust-forming radius. The inclusion of vibrationally excited levels will be the subject of future work.

4.3 Fitting the molecular emission-line fluxes

Having obtained estimates for the inner radius, radial density and temperature variations of the dust (Section 4.1), these were used as the starting points for modelling the molecular gas using SMMOL, iterating until an overall fit to the ^{12}CO and ^{13}CO line fluxes was obtained, primarily by varying the gas density $n(\mathrm{H}_2)(r)$ and the gas radial temperature and velocity profiles, $T(r)$ and $v(r)$.

The radius at which H_2O molecules condense on to dust grains, i.e. below the sublimation temperature of water-ice, was estimated to be 6.9×10^{16} cm, well inside the outer radius of 2.9×10^{17} cm adopted for our model, so the depletion of gaseous H_2O by this effect was incorporated into the modelling. CO has a much lower sublimation temperature, so depletion of CO on to grains did not have to be taken into account. The penetration of interstellar UV photons can dissociate molecules in the outer regions of the outflow. To estimate the water dissociation radius, the method described by

Decin et al. (2006) was used, while for CO, the approach followed by Mamon, Glassgold & Huggins (1988) was used. For CO, we found that due to shielding by dust in the outflow the dissociation radius was outside the outer radius of 2.9×10^{17} cm of the model. The predicted non-dissociation of CO is consistent with the non-detection in our SPIRE FTS spectrum of the atomic carbon [C I] lines at 492 and 809 GHz. The predicted dissociation radius for H_2O molecules was 2.0×10^{17} cm, just inside the outer radius of the model but this did not have to be taken into account since all the gaseous water molecules had already been depleted on to dust grains beyond 6.9×10^{16} cm.

A turbulent velocity of 1.0 km s^{-1} was adopted based upon Multi-Element Radio-Linked Interferometer Network observations of water maser clouds in VY CMa, which suggest a turbulent width of 1.0 km s^{-1} (Richards et al. 1998). The initial wind radial velocity law was based upon maser observations (Richards et al. 1998) and CO line observations (Decin et al. 2006, and references therein). We constrained the outflow model first using the CO observations and the best-fitting CO model was then used as the starting point for the modelling of the H_2O and SiO line data, with $T(r)$ and $v(r)$ again being varied until a best fit was obtained for all of the molecular species. The structure of the outflow found from the best-fitting CO and H_2O models did indeed match.

The NLTE model line intensities for ^{12}CO, ^{13}CO and SiO are plotted in the previously discussed spectral line energy distribution diagrams (Figs 3, 4 and 6, respectively), whereas the modelled and observed H_2O lines are compared via spectral plots, since H_2O line intensities do not follow a simple curve in a spectral line energy distribution diagram. Fig. 7 (para-H_2O) and Fig. 8 (ortho-H_2O) show the model spectra for 25 different H_2O lines overlaid on the SPIRE observations of the lines. The model spectra have been convolved to the apodized instrumental resolution, since the observed lines are unresolved.

We have estimated the χ^2 goodness of fit, defined by $\chi^2 = \Sigma((O_i - P_i)^2/\sigma_i^2)/n$, where O_i is the SPIRE line intensity, P_i is the SMMOL-predicted line intensity and n is the number of degrees of freedom. The uncertainty σ_i in an observed line flux was adopted to be 20 per cent of the observed flux, accounting the difference of the

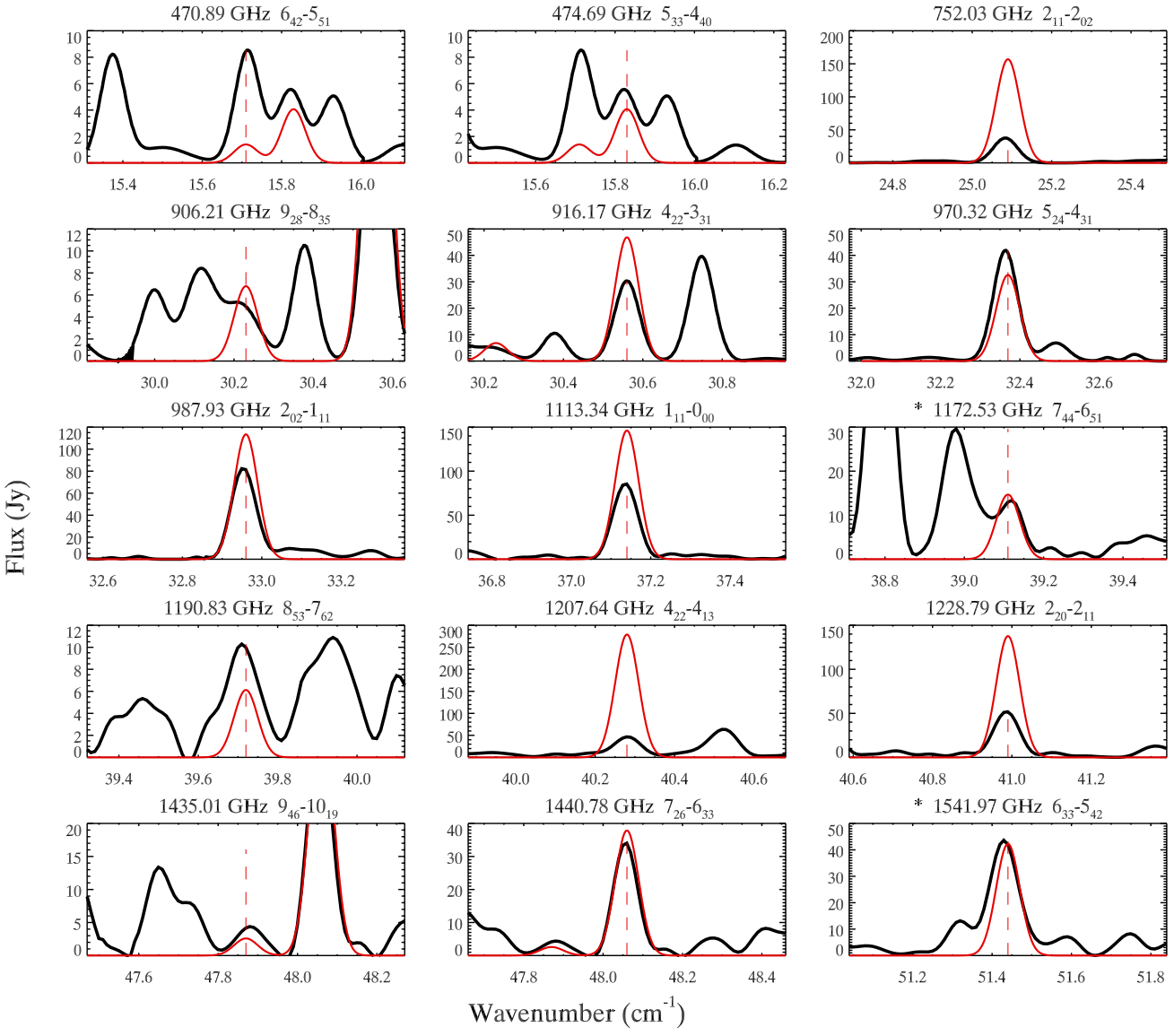

Figure 7. SMMOL fits to the para-H_2O lines observed by SPIRE. The OD 123 spectra are plotted in bold black while the model spectra are in red. The frequencies of the lines, denoted by vertical dashes, are given at the top of the panels.

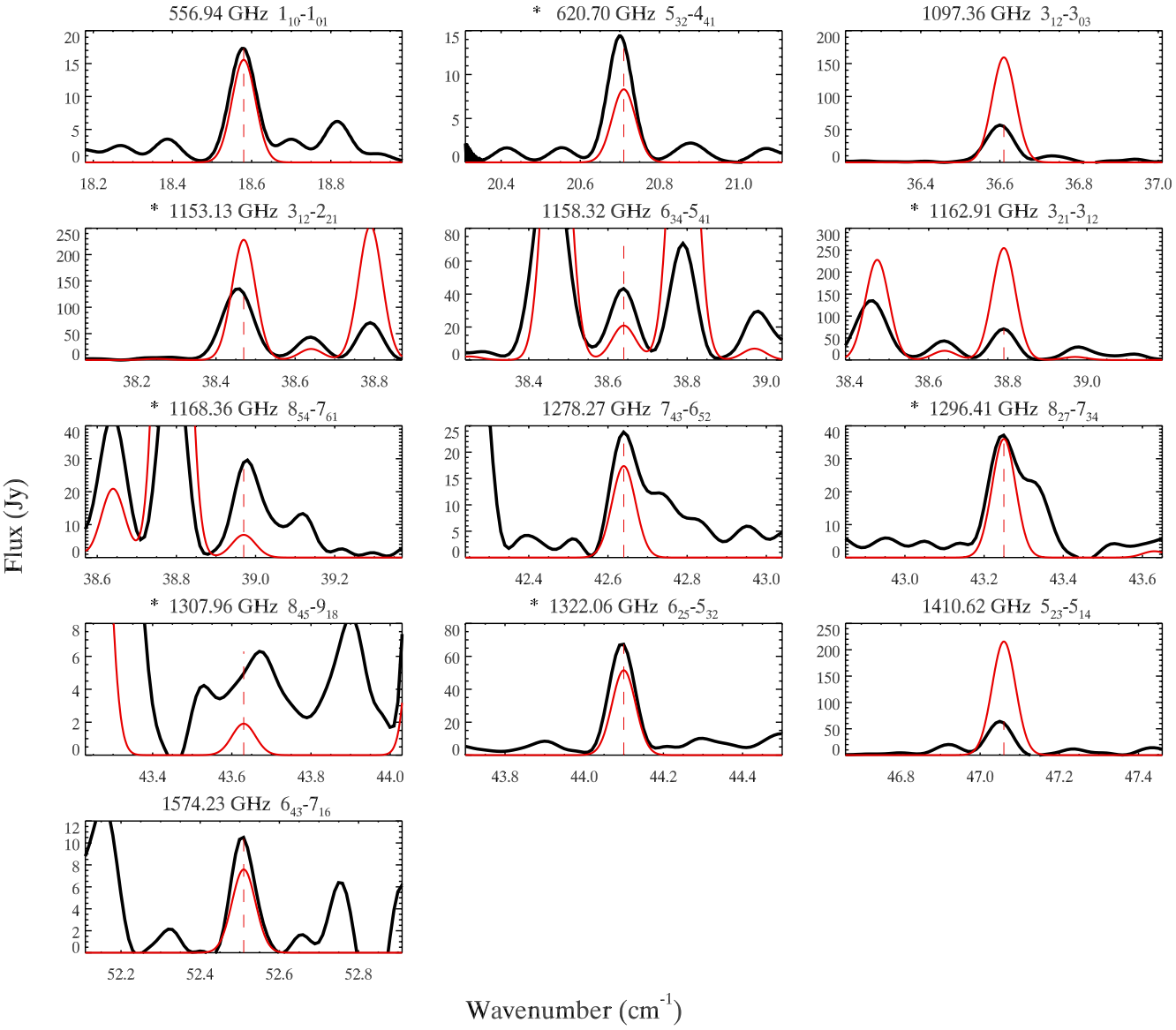

Figure 8. SMMOL fits to the ortho-H_2O lines observed by SPIRE. The OD 123 spectra are plotted in black while the model spectra are in red. The frequencies of the lines, denoted by vertical dashes, are given at the top of the panels.

Table 3. Reduced χ^2 values for the SMMOL model fits to the observed lines, together with mean and median I_{obs}/I_{SMMOL} ratios.

Molecules	χ^2_{red} SPIRE		χ^2_{red} PACS	Mean of $\frac{I_{obs}}{I_{SMMOL}}$			Median of $\frac{I_{obs}}{I_{SMMOL}}$		
	OD 123	OD 317	OD 173	OD 123	OD 317	OD 173	OD 123	OD 317	OD 173
CO SPIRE only	0.12	0.26		1.03 ± 0.21	0.97 ± 0.30		1.01	0.93	
PACS only			0.94			0.65 ± 0.11			0.69
SPIRE + PACS (OD 173)	0.27	0.30		0.86 ± 0.26	0.83 ± 0.28		0.84	0.80	
^{13}CO	0.67	0.83		1.05 ± 0.62	0.84 ± 0.55		1.15	0.80	
SiO	0.16	0.34		1.01 ± 0.31	0.86 ± 0.35		1.10	0.94	
Para-H_2O	4.34	4.57		1.00 ± 0.56	0.92 ± 0.51		0.93	0.86	
Ortho-H_2O	4.96	3.19		1.54 ± 1.20	1.60 ± 1.12		1.40	1.47	

measured line intensities between OD 123 and 317. Table 3 summarizes the χ^2 values obtained for the different molecular species. CO and SiO show the best fits. Table 3 also summarizes the observed-to-predicted line flux ratios for the different molecular species that were modelled.

Our overall best-fitting model (see Table 2 and Fig. 9) required a gas-to-dust mass ratio of 267, with a gas acceleration zone (to a terminal velocity of 44 km s^{-1}) located at the dust condensation radius at 9R_*, beyond which the total mass-loss rate in the region labelled as the 'higher mass-loss rate zone' in Fig. 9 is 1.85×10^{-4} $M_\odot$ yr^{-1},

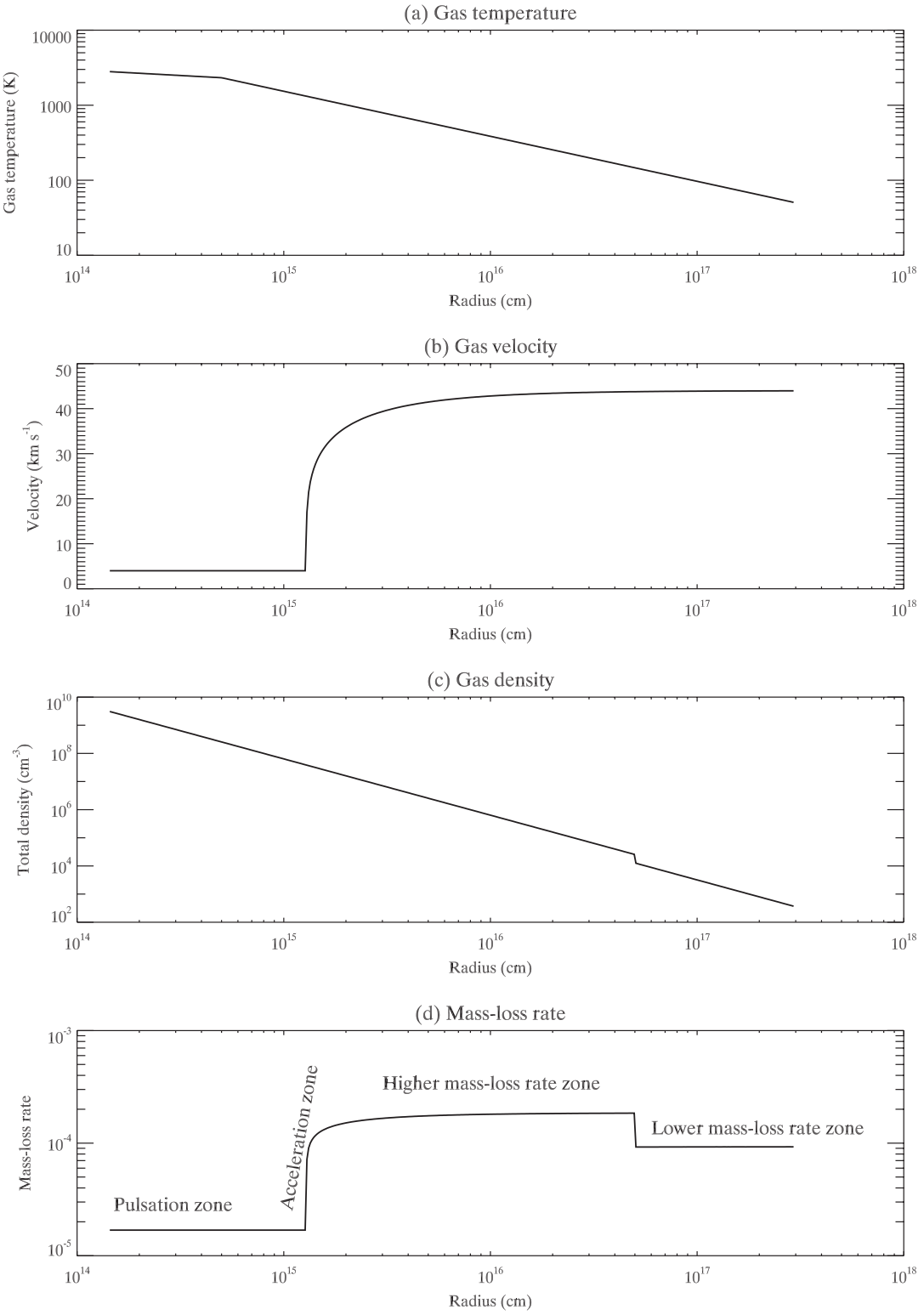

Figure 9. The wind structure required by the best-fitting SMMOL model, whose parameters are listed in Table 2.

dropping by a factor of 2, to $9.5 \times 10^{-5}\,M_{\odot}\,yr^{-1}$, beyond a radius $R_{outflow,break} \sim 350R_{*}$.

The model required a wind with a two-component radial temperature profile. The higher excitation rotational lines of water required a flat ($\alpha \sim 0.1$–0.15) radial power-law temperature profile from the stellar photosphere out to (1.0–1.3) $\times\ 10^{15}$ cm (7–9 R_{*}), close to the radius of the dust condensation zone suggested by our dust radiative transfer calculations. Beyond there, the CO lines and the lower excitation water lines could be fitted with an $r^{-0.5}$ temperature distribution. Initial attempts were made to use a single radial temperature profile for the CO and H_2O models but in both cases too little flux was produced in high-J CO transitions and high-E_{up}

Table 4. Observed and predicted H_2O line fluxes in the SPIRE wavelength range, with model predictions for population inversion and masing in these lines.

Spectral line			Transition	E_{up}	Obs int.[a]		SMMOL		Obs/Pred.[b]	
ν_0 (GHz)	ν_0 (cm^{-1})	λ_0 (μm)	$J'_{K'_a K'_c}$–$J_{K_a K_c}$	(cm^{-1})	I_{obs} (OD 123) (10^{-18} W cm^{-2})	I_{obs} (OD 317) (10^{-18} W cm^{-2})	I^c_{SMMOL}	Inverted?[d]	I_{obs}/I_{SMMOL} OD 123	OD 317
Para-H_2O										
470.8958	15.707	636.66	6_{42}–5_{51}	757.78	221.8	135.7	31.1	Y	7.1	4.4
474.7033	15.834	631.55	5_{33}–4_{40}	503.97	159.5	137.9	90.8	Y	1.8	1.5
752.0483	25.086	398.64	2_{11}–2_{02}	95.18	959.7	769.8	3503.0	N	0.3	0.2
906.2355	30.229	330.82	9_{28}–8_{35}	1080.39	196.2	131.1	151.9	Y	1.3	0.9
916.1888	30.561	327.23	4_{22}–3_{31}	315.78	788.2	664.4	1045.5	Y	0.8	0.6
970.3327	32.367	308.97	5_{24}–4_{31}	416.21	871.6	999.3	727.8	Y	1.2	1.4
987.9609	32.955	303.45	2_{02}–1_{11}	70.09	1912.0	1856.0	2533.3	N	0.8	0.7
1113.3673	37.138	269.27	1_{11}–0_{00}	37.14	2014.0	2040.0	3262.7	N	0.6	0.6
1172.5479	39.112	255.68	7_{44}–6_{51}	927.74	304.4	291.0	327.7	Y(w)	0.9	0.9
1190.8655	39.723	251.75	8_{53}–7_{62}	1255.91	260.3	229.6	136.7	N	1.9	1.7
1207.6845	40.284	248.24	4_{22}–4_{13}	315.78	1187.0	1119.0	6230.1	Y	0.2	0.2
1228.8202	40.989	243.97	2_{20}–2_{11}	136.16	1297.0	1271.0	3075.7	N	0.4	0.4
1435.0526	47.868	208.91	9_{46}–10_{19}	1340.88	107.3	100.0	57.8	N	1.9	1.7
1440.8088	48.060	208.08	7_{26}–6_{33}	709.61	775.9	725.2	845.6	Y	0.9	0.9
1542.0214	51.436	194.42	6_{33}–5_{42}	661.55	1129.0	1146.0	944.1	N	1.2	1.2
Ortho-H_2O										
448.0012	14.944	669.18	4_{23}–3_{30}	300.36	–[e]	389.5	180.3	Y	–	2.2
556.9384	18.577	538.30	1_{10}–1_{01}	42.37	486.0	393.9	348.0	N	1.4	1.1
620.7059	20.705	483.00	5_{32}–4_{41}	508.81	378.6	372.3	185.8	Y	2.0	2.0
1097.3879	36.605	273.19	3_{12}–3_{03}	173.37	1317.0	1382.0	3560.4	Y	0.4	0.4
1153.1508	38.465	259.98	3_{12}–2_{21}	173.37	1953.0	2367.0	5092.8	Y	–[f]	–[f]
1158.3673	38.639	258.81	6_{34}–5_{41}	648.98	1063.0	1025.0	466.5	Y(w)	2.3	2.2
1162.9117	38.791	257.79	3_{21}–3_{12}	212.16	1673.0	1635.0	5691.6	Y(vw)	0.3	0.3
1168.3805	38.973	256.59	8_{54}–7_{61}	1255.17	666.7	668.9	153.7	Y	4.3	4.4
1278.2872	42.639	234.53	7_{43}–6_{52}	931.24	587.2	570.3	387.8	Y	1.5	1.5
1296.4552	43.245	231.25	8_{27}–7_{34}	885.60	907.1	821.1	804.5	Y	1.1	1.0
1307.9976	43.630	229.21	8_{45}–9_{18}	1122.71	135.2	102.3	42.7	Y	3.2	2.4
1322.0648	44.099	226.76	6_{25}–5_{32}	552.91	1647.0	1492.0	1150.9	Y(vw)	1.4	1.3
1410.6491	47.054	212.53	5_{23}–5_{14}	446.51	1512.0	2989.0	4815.6	Y	0.3	0.6
1574.2321	52.510	190.44	6_{43}–7_{16}	756.72	232.9	–[e]	169.5	Y	1.4	–

[a]Observed line intensities (OD 123). [b]The ratio of the observed-to-predicted line fluxes. [c]SMMOL predicted line intensities. [d]SMMOL prediction for population inversion: Y (yes) or N (no). Y(w) indicates population inversion, but weakly. [e]The line was out of the spectral coverage. [f]Blended with CO $J = 10$–9.

H_2O transitions, although they successfully reproduced the lower transitions. We detected strong vibrationally excited lines of water in our *Herschel* spectra, which require temperatures in excess of 1000 K to be significantly populated by collisions. Such lines will also be optically thick and it is this that maintains a relatively flat temperature profile, because heat cannot easily escape by radiative processes. However, once the gas cools to about 1000 K, the vibrational states are no longer collisionally excited, thus removing a large source of opacity and allowing photons to escape. At this point the radial profile adopts the expected $r^{-0.5}$ profile. This behaviour was first predicted by Goldreich & Scoville (1976, fig. 2). This sudden cooling effect due to loss of opacity can trigger the formation of dust particles in the outflow, which up to then had been driven by radiation pressure acting through the opacity of vibrationally excited water.

The modelling of our *Herschel* CO and H_2O line data for VY CMa (Fig. 3 for CO and Figs 7–8 for H_2O) is consistent with VY CMa having undergone mass-loss enhancements in the past (Richards et al. 1998; Decin et al. 2006). Fig. 9 shows the mass-loss rate history of VY CMa that provided the calculated molecular emission fluxes most consistent with our observations. Starting from the right-hand side (the older and outer part of the outflow), there was a phase of lower mass-loss that ended 360 yr ago, when the mass-loss rate doubled to 1.85×10^{-4} $M_\odot$ yr^{-1} (the 'higher mass-loss rate zone'). The acceleration zone is interpreted as caused by radiative pressure on newly formed dust grains, followed by momentum transfer to the gas via collisions with dust grains.

The modelling of the water lines used an ortho:para ratio of 3:1 and included masing in the calculation of the level populations. In general, our NLTE models with masing included can fit the observed H_2O line intensities, but the 470.9 GHz ortho-H_2O line is a clear outlier (Table 4) and was omitted in the evaluation of the χ^2, and mean and median observed/predicted line flux ratios for H_2O presented in Table 3. Inspection of those mean and median ratios indicates that the assumption of a 3:1 ortho:para ratio is consistent with the observations. The early NLTE analysis of Royer et al. (2010) obtained an H_2O ortho:para ratio of 1.3:1. We attribute the difference between the two ratios to the fact that Royer et al.'s model was more suited to optically thin regimes, whereas SMMOL is designed to handle large optical depths and includes maser effects.

The LTE analysis of the SiO lines clearly showed a temperature structure with at least two components (Fig. 6). This was confirmed by our NLTE radiative transfer modelling of the CO and H_2O lines. The inferred relatively flat radial temperature profile out to 7–9 stellar radii, coupled with the detection of strong vibrationally excited water lines, indicates the existence of a region where opacity from vibrationally excited lines traps the radiation and prevents radiative cooling of the gas, confirming the existence of the flat inner

radial temperature profiles predicted by Goldreich & Scoville. The modelling of SiO required a significant abundance drop at the dust-forming region, consistent with a large fraction of SiO molecules condensing into silicate dust grains. Our model assumes a factor of 20 reduction in the density of SiO.

4.4 Masing and lasing transitions of water vapour

For the water lines modelled with SMMOL, our NLTE radiative transfer calculations allowed us to infer which ones should be undergoing masing action. Table 4 lists the H_2O transitions which are predicted by our best-fitting SMMOL model to have inverted energy populations and to be undergoing masing action (70 per cent). For ease of comparison, the observed line fluxes included in the table are from the OD123 SPIRE FTS observations only. Our best-fitting model predicts 6 masing lines below 1000 GHz and 14 lasing lines above 1000 GHz, so the widespread occurrence of masing or lasing action by water molecules in the outflow is expected. This is consistent with the predictions of Deguchi & Watson (1989) and Neufeld & Melnick (1991), who used line escape probability techniques, and of Doty & Neufeld (1997) and Yates et al. (1997), who both used ALI techniques to model the line radiative transfer.

Higher spectral resolution observations could test whether maser action is occurring for the predicted lines. Velocity-resolved line profiles have been already measured for three of the lines that are predicted to be masing. From *Herschel* HIFI observations of VY CMa, Harwit et al. (2010) found the H_2O 5_{32}–4_{41} transition at 620.70 GHz (20.70 cm^{-1}) to show a very narrowly peaked line profile, suggesting non-thermal maser emission. Ground-based APEX observations by Menten et al. (2008) of the para-H_2O 6_{42}–5_{51} transition at 470.889 GHz (15.70 cm^{-1}) and the 5_{33}–4_{40} transition at 474.680 GHz (15.83 cm^{-1}) showed several narrow emission peaks superposed on a broader overall emission profile.

Humphreys et al. (1997) suggested the detection SiO $v = 1$ and $v = 2$ $J = 7$–6 and 8–7 maser emission from VY CMa. Our SMMOL models for SiO predict that $v = 0$ low-J transitions (up to $J = 7$–6) should be strongly masing, but for higher levels, population inversions are not predicted. The inversions predicted for low-J SiO levels are consistent with the strongly polarized $v = 0$ $J = 1$–0 SiO emission found by McIntosh & Rislow (2009), indicating masing. Caution is required however, as the future inclusion of vibrationally excited SiO transitions in the models could change the predictions for high-J $v = 0$ SiO lines.

5 SUMMARY

The fluxes of eight ^{12}CO line present in the 54–210-μm *Herschel* PACS spectrum of VY CMa have been measured, along with the fluxes of more than 260 emission lines present in the SPIRE FTS 190–650 μm spectrum. Many lines are identified with H_2O transitions. Other identified molecules include CO, ^{13}CO, $H_2^{18}O$, SiO, HCN, SO, SO_2, CS, H_2S and NH_3. LTE excitation temperatures have been derived for CO, ^{13}CO, HCN and SiO, while NLTE modelling has been carried out for the ^{12}CO lines in the PACS and SPIRE spectra, and for the ^{13}CO, H_2O and SiO lines in the SPIRE FTS spectra.

Our LTE and NLTE analyses have shown the following.

(i) Corresponding transitions of ^{12}CO and ^{13}CO in the SPIRE FTS spectrum have a flux ratio of 7.0 ± 1.8. These lines can be fitted with an LTE excitation temperature of 350 ± 90 K and a $^{12}C/^{13}C$ ratio of 6.2 ± 2.0. Our best-fitting NLTE model yields a $^{12}C/^{13}C$ ratio of 5.6 ± 1.8, much lower than previously derived from ground-based measurements of lower-J lines but consistent with $^{12}C/^{13}C$ ratios measured previously for other M-supergiants.

(ii) More than 20 pure rotational transitions of SiO were detected in the SPIRE FTS spectra. The spectral line energy distribution of these lines clearly shows two SiO temperature components: one at ∼1000 K and the other at ∼200 K. The first appears to correspond to the region between the photosphere and the dust condensation radius, and the latter to the region of the circumstellar envelope beyond the dust condensation radius.

(iii) HCN was detected in the *Herschel* spectra, as already known from ground-based millimetre wavelength observations. The formation process for HCN in an oxygen-rich circumstellar envelopes is still uncertain, with the two main candidates being photon-mediated processes in the outer circumstellar envelope and shock chemistry in the stellar atmosphere and inner wind. The low excitation temperature (250 K) that we derive for HCN, lower even than that of CO, favours the first of these mechanisms.

(iv) Our best-fitting NLTE model for ^{12}CO, ^{13}CO and H_2O yields an overall mass-loss rate of 1.85×10^{-4} $M_\odot$ yr^{-1} between radii of $9R_*$ and $350R_*$, dropping by a factor of 2 beyond that. It requires a flat temperature profile below the dust condensation radius, consistent with the H_2O opacity preventing coolant lines from escaping, while beyond that point the gas temperature follows an $r^{-0.5}$ dependence (as predicted by Goldreich & Scoville 1976), consistent with the lines having become optically thin.

(v) The NLTE H_2O line modelling predicts that many of the lines in the SPIRE frequency band should be masing. The observed fluxes alone are not sufficient to confirm masing in the lines, although previously published high spectral resolution observations have indicated maser action in at least one of the lines.

ACKNOWLEDGEMENTS

SPIRE has been developed by a consortium of institutes led by Cardiff University (UK) and including University of Lethbridge (Canada); NAOC (China); CEA, LAM (France); IFSI, University of Padua (Italy); IAC (Spain); Stockholm Observatory (Sweden); Imperial College London, RAL, UCL-MSSL, UKATC, University of Sussex (UK); and Caltech, JPL, NHSC, University of Colorado (USA). This development has been supported by national funding agencies: CSA (Canada); NAOC (China); CEA, CNES, CNRS (France); ASI (Italy); MCINN (Spain); SNSB (Sweden); STFC and UKSA (UK); and NASA (USA). PACS has been developed by a consortium of institutes led by MPE (Germany) and including UVIE (Austria); KU Leuven, CSL, IMEC (Belgium); CEA, LAM (France); MPIA (Germany); INAF-IFSI/OAA/OAP/OAT, LENS, SISSA (Italy); IAC (Spain). This development has been supported by the funding agencies BMVIT (Austria), ESA-PRODEX (Belgium), CEA/CNES (France), DLR (Germany), ASI/INAF (Italy) and CICYT/MCYT (Spain). PvH acknowledges support from the Belgian Science Policy office through the ESA PRODEX programme.

REFERENCES

Barber R. J., Tennyson J., Harris G. J., Tolchenov R. N., 2006, MNRAS, 368, 1087

Barlow M. J. et al., 1996, A&A, 315, L241

Beichman C. A., Neugebauer G., Habing H. J., Clegg P. E., Chester T. J., 1988, Infrared Astronomical Satellite (IRAS) Catalogs and Atlases, NASA RP-1190, Vol. 1. NASA, Washington

Biermann P., Harwit M., 1980, ApJ, 241, L105

Charnley S. B., Tielens A. G. G. M., Kress M. E., 1995, MNRAS, 274, L53

Choi Y. K. et al., 2008, PASJ, 60, 1007
Clegg P. E. et al., 1996, A&A, 315, L38
Danchi W. C., Bester M., Degiacomi C. G., Greenhill L. J., Townes C. H., 1994, AJ, 107, 1469
Dayou F., Balança C., 2006, A&A, 459, 297
De Beck E., Decin L., De Koter A., Justtanont K., Verhoelst T., Kemper F., Menten K. M., 2010, A&A, 523, A18
de Graauw T. T. G. et al., 2010, A&A, 518, L6
Decin L., Hony S., Koter A. D., Justtanont K., Tielens A. G. G. M., Waters L. B. F. M., 2006, A&A, 456, 549
Deguchi S., Goldsmith P. F., 1985, Nat, 317, 336
Deguchi S., Nguyen-Q-Rieu, 1990, ApJ, 360, L27
Deguchi S., Watson W. D., 1989, ApJ, 340, L17
Doty S. D., Neufeld D. A., 1997, ApJ, 489, 122
Draine B. T., Lee H. M., 1984, ApJ, 285, 89
Duari D., Cherchneff I., Willacy K., 1999, A&A, 341, L47
Efstathiou A., Rowan-Robinson M., 1990, MNRAS, 245, 275
Ercolano B., Barlow M. J., Storey P. J., 2005, MNRAS, 362, 1038
Faure A., Josselin E., 2008, A&A, 492, 257
Fulton T. R. et al., 2010, in Oschmann J. M., Jr, Clampin M. C., MacEwen H. A., eds, Proc. SPIE Vol. 7731, Space Telescopes and Instrumentation 2010: Optical, Infrared, and Millimeter Wave. SPIE, Bellingham, p. 773134
Fulton T. R. et al., 2008, in Oschmann J. M., Jr, de Graauw M. W. M., MacEwen H. A., eds, Proc. SPIE Vol. 7010, Astronomical Telescopes and Instrumentation: Synergies Between Ground and Space. SPIE, Bellingham, p. 70102T
Goldreich P., Scoville N., 1976, ApJ, 205, 144
Goldsmith P. F., Langer W. D., 1999, ApJ, 517, 209
Green S., Maluendes S., McLean A. D., 1993, ApJS, 85, 181
Griffin M. J. et al., 2010, A&A, 518, L3
Groenewegen M. A. T. et al., 2011, A&A, 526, 162
Harwit M. et al., 2010, A&A, 521, L51
Humphreys E. M. L., Gray M. D., Yates J. A., Field D., 1997, MNRAS, 287, 663
Humphreys R. M., Helton L. A., Jones T. J., 2007, AJ, 133, 2716
Ireland M. J., Scholz M., Wood P. R., 2011, MNRAS, 418, 114
Jewell P. R., Snyder L. E., Schenewerk M. S., 1986, Nat, 323, 311
Justtanont K. et al., 2000, A&A, 360, 1117
Justtanont K. et al., 2012, A&A, 537, A144
Kaminski T. et al., 2013, A&A, 551, A113
Kaufman M. J., Neufeld D. A., 1996, ApJ, 456, 611
Kemper F., Stark R., Justtanont K., De Koter A., Tielens A. G. G. M., Waters L. B. F. M., Cami J., Dijkstra C., 2003, A&A, 407, 609
Langhoff S. R., Bauschlicher C. W., 1993, Chem. Phys. Lett., 211, 305
Lerate M. R., Yates J. A., Barlow M. J., Viti S., Swinyard B. M., 2010, MNRAS, 406, 2445
Mamon G. A., Glassgold A. E., Huggins P. J., 1988, ApJ, 328, 797
Mathis J. S., Rumpl W., Nordsieck K. H., 1977, ApJ, 217, 425
Matsuura M., Yamamura I., Cami J., Onaka T., Murakami H., 2002, A&A, 383, 972
McIntosh G. C., Rislow B., 2009, ApJ, 692, 154
Menten K. M., Young K., 1995, ApJ, 450, L67
Menten K. M., Philipp S. D., Güsten R., Alcolea J., Polehampton E. T., Brünken S., 2006, A&A, 454, L107
Menten K. M., Lundgren A., Belloche A., Thorwirth S., Reid M. J., 2008, A&A, 477, 185
Menten K. M. et al., 2010, A&A, 521, L7
Milam S. N., Woolf N. J., Ziurys L. M., 2009, ApJ, 690, 837
Monnier J. D., Tuthill P. G., Lopez B., Cruzalebes P., Danchi W. C., Haniff C. A., 1999, ApJ, 512, 351
Müller H. S. P., Schlöder F., Stutzki J., Winnewisser G., 2005, J. Mol. Struct., 742, 215
Muller S., Dinh-V-Trung L. J., Hirano N., Muthu C., Kwok S., 2007, ApJ, 656, 1109
Naylor D. A., Tahic M. K., 2007, J. Opt. Soc. Am. A, 24, 3644
Nercessian E., Omont A., Benayoun J. J., Guilloteau S., 1989, A&A, 210, 225
Neufeld D. A., Melnick G. J., 1991, ApJ, 368, 215
Neufeld D. A., Feuchtgruber H., Harwit M., Melnick G. J., 1999, ApJ, 517, L147
Ott S., 2010, in Yoshihiko M., Koh-Ichiro M., Masatoshi O., eds, ASP Conf. Ser. Vol. 434, Astronomical Data Analysis Software and Systems XIX. Astron. Soc. Pac., San Francisco, p. 139
Pickett H. M., 1991, J. Mol. Spectrosc., 148, 371
Pickett H. M., Poynter R. L., Cohen E. A., Delitsky M. L., Pearson J. C., Müller H. S. P., 1998, J. Quant. Spectrosc. Radiat. Transfer, 60, 883
Pilbratt G. L. et al., 2010, A&A, 518, L1
Poglitsch A. et al., 2010, A&A, 518, L2
Polehampton E. T., Menten K. M., van der Tak F. F. S., White G. J., 2010, A&A, 510, 80
Rawlings J. M. C., Yates J. A., 2001, MNRAS, 326, 1423
Richards A. M. S., Yates J. A., Cohen R. J., 1998, MNRAS, 299, 319
Rothman L. S. et al., 2009, J. Quant. Spectrosc. Radiat. Transfer, 110, 533
Royer P. et al., 2010, A&A, 518, L145
Rybicki G. B., Hummer D. G., 1991, A&A, 245, 171
Sauval A. J., Tatum J. B., 1984, ApJS, 56, 193
Scharmer G. B., Carlsson M., 1985, J. Comput. Phys., 59, 56
Sidaner P. L., Le Bertre T., 1996, A&A, 314, 896
Sloan G. C., Kraemer K. E., Price S. D., Shipman R. F., 2003, ApJS, 147, 379
Swinyard B. M. et al., 2010, A&A, 518, L4
Tenenbaum E. D., Dodd J. L., Milam S. N., Woolf N. J., Ziurys L. M., 2010, ApJS, 190, 348
Tsuji T., Ohnaka K., Aoki W., Yamamura I., 1997, A&A, 320, L1
Wesson R. et al., 2010, A&A, 518, L144
Willacy K., Millar T. J., 1997, A&A, 324, 237
Yang B., Stancil P. C., Balakrishnan N., Forrey R. C., 2010, ApJ, 718, 1062
Yates J. A., Field D., Gray M. D., 1997, MNRAS, 285, 303
Ziurys L. M., Milam S. N., Apponi A. J., Woolf N. J., 2007, Nat, 447, 1094
Ziurys L. M., Tenenbaum E. D., Pulliam R. L., Woolf N. J., Milam S. N., 2009, ApJ, 695, 1604

APPENDIX A: LINE FLUXES AND LINE IDENTIFICATIONS

Table A1. VY CMa: CO line fluxes in the PACS spectra.

PACS $\bar{\lambda}_{obs}$ (μm)	$\bar{\nu}_{obs}$ (cm^{-1})	$F(\times 10^{-18}$ W m$^{-2})$	ID $\bar{\nu}_o$ (cm^{-1})	$\bar{\nu}_o$ (GHz)	$\bar{\lambda}_o$ (μm)	Transition
186.02	53.758	1479 ± 69	53.764	1611.78	186.00	CO 14–13
173.65	57.587	1495 ± 57	57.593	1726.59	173.63	CO 15–14
162.83	61.412	1402 ± 153	61.421	1841.33	162.81	CO 16–15
153.28	65.239	1740 ± 75	65.246	1956.00	153.27	CO 17–16
144.79	69.065	1755 ± 182	69.068	2070.60	144.78	CO 18–17
137.23	72.870	1273 ± 122	72.888	2185.12	137.20	CO 19–18
124.19	80.520	972 ± 188	80.560	2413.90	124.19	CO 21–20
118.60	84.317	1441 ± 164	84.331	2528.15	118.58	CO 22–21

Table A2. VY CMa line fluxes (F) and identifications (IDs) in the SPIRE FTS SLW spectra. Only the first 15 lines of the table are indicated, and the rest is found in the on-line version. An ID row beginning with a '+' indicates that the line is blended with that on the row above. ν_0 (cm^{-1}) and λ_0 (μm) are vacuum wavenumbers and wavelengths, respectively. The quantum numbers given in the 'transition' column are J except where stated. H_2O transitions are given in the format $J'_{K'_a K'_c}$–$J_{K_a K_c}$. The listed uncertainties for the line fluxes are those from the line fitting, and absolute calibration uncertainties are not included.

OD123		OD317		ID				
$\bar{\nu}_{obs}$ (cm^{-1})	$F(\times10^{-18}$ W m$^{-2})$	$\bar{\nu}_{obs}$ (cm^{-1})	$F(\times10^{-18}$ W m$^{-2})$	ν_0 (cm^{-1})	ν_0 (GHz)	λ_0 (μm)	Species	Transition
		14.931 ± 0.003	389.5 ± 32.2	14.944	448.00	669.18	o-H_2O	4_{23}–3_{30}
15.374	210.3 ± 8.1	15.371 ± 0.001	190.0 ± 67.8	15.379	461.05	650.24	CO	4–3
15.501	60.2 ± 9.0	15.538 ± 0.005	80.0 ± 4.8	15.489	464.35	645.62	p-H_2O?	$\nu_1 = 1{,}5_{33}$–3_{44}
				+15.501	464.71	645.11	SiS?	$v = 3$, 26–25
				+15.505	464.83	644.96	p-H_2O?	$\nu_1 = 1{,}10_{37}$–$11_{2\,10}$
15.714	221.8 ± 4.9	15.707 ± 0.001	135.7 ± 2.4	15.707	470.88	636.66	p-H_2O	6_{42}–5_{51}
15.823	159.5 ± 7.1	15.826 ± 0.001	137.9 ± 2.5	15.834	474.69	631.55	p-H_2O	5_{33}–4_{40}
				+15.817	474.18	632.23	SiO	$v = 1$, 11–10
				+15.830	474.57	631.73	SO	11_{12}–10_{11}
15.932	137.2 ± 5.3	15.924 ± 0.001	109.9 ± 2.5	15.930	477.57	627.75	SiO	11–10
16.105	44.6 ± 2.0	16.056 ± 0.018	8.8 ± 2.5	16.096	482.55	621.26	SiS?	$v = 3$, 27–26
				+16.100	482.67	621.13	CS?	$v = 2$, 10–9
				+16.105	482.82	620.94	$Si^{33}S$?	27–26
16.333	38.9 ± 1.9	16.315 ± 0.004	23.1 ± 1.9	16.335	489.71	612.18	SiS?	27–26
				+16.336	489.74	612.13	CS?	10–9
16.626	28.1 ± 2.6	16.605 ± 0.017	15.3 ± 2.6	16.628	498.49	601.40	^{29}SiS?	28–27
				+16.628	498.49	601.39	p-H_2O?	$\nu_2 = 1{,}7_{44}$–6_{51}
16.713	53.1 ± 2.5			16.700	500.65	598.81	$Si^{33}S$?	28–27
16.937	51.8 ± 3.0	16.946 ± 0.004	64.3 ± 2.4	16.934	507.67	590.54	o-H_2O?	$\nu_2 = 1{,}\nu_3 = 1{,}10_{82}$–$9_{91}$
				+16.939	507.82	590.36	SiS?	28–27

Table A3. VY CMa: Line fluxes and identifications in the SPIRE FTS SSW spectra. Only the first 19 lines of the table are indicated, and the rest is found in the online version.

OD123		OD317		ID				
$\bar{\nu}_{obs}$ (cm^{-1})	$F(\times10^{-18}$ W m$^{-2})$	$\bar{\nu}_{obs}$ (cm^{-1})	$F(\times10^{-18}$ W m$^{-2})$	ν_0 (cm^{-1})	ν_0 (GHz)	λ_0 (μm)	Species	Transition
32.624	35.5 ± 6.2	32.624 ± 0.009	45.2 ± 10.1	32.637	978.43	306.40	o-H_2O?	$\nu_3 = 2$, 7_{52}–6_{61}
				+32.641	978.55	306.37	CS?	20–19
32.698	87.7 ± 6.1	32.690 ± 0.006	79.6 ± 10.0	32.688	979.96	305.92	SiS?	$v = 3$,55–54
				+32.708	980.56	305.74	$Si^{33}S$?	55–54
32.832	37.8 ± 5.4			32.850	984.82	304.41	^{29}SiO?	23–22
				+32.851	984.85	304.40	$Si^{34}S$?	56–55
32.955	1912.0 ± 6.4	32.949 ± 0.001	1856.0 ± 9.0	32.954	987.94	303.45	p-H_2O	2_{02}–1_{11}
33.069	212.2 ± 6.9	33.061 ± 0.002	205.0 ± 6.3	33.067	991.32	302.42	^{13}CO	9–8
33.140	170.1 ± 6.9	33.132 ± 0.002	150.7 ± 6.8	33.155	993.96	301.62	^{29}SiS?	56–55
				+33.156	993.99	301.60	^{30}SiS?	57–56
				+33.1	992.31	301.6	NH_3?	Several lines
33.271	183.8 ± 5.3	33.260 ± 0.001	170.5 ± 4.7	33.270	997.41	300.57	SiO	23–22
33.408	68.1 ± 21.0	33.393 ± 0.015	21.8 ± 13.2	33.385	1000.86	299.54	p-H_2O?	$\nu_2 = 2$, 2_{11}–2_{02}
				+33.388	1000.95	299.51	o-H_2O?	$15_{4\,11}$–$16_{3\,14}$
				33.407	1001.52	299.34	o-H_2O?	$\nu_3 = 2$, 5_{32}–4_{41}
33.464	80.0 ± 20.6	33.437 ± 0.006	71.9 ± 12.0	33.433	1002.30	299.10	$Si^{34}S$?	57–56
				+33.466	1003.29	298.81	o-$H_2^{18}O$	5_{24}–4_{31}
33.621	87.8 ± 5.3	33.617 ± 0.003	61.7 ± 4.7	33.608	1007.54	297.55	SiS?	$v = 1$,56–55
				+33.649	1008.77	297.19	^{13}CS?	$v = 1$,22–21
33.766	68.4 ± 5.4	33.762 ± 0.006	24.6 ± 4.8	33.742	1011.56	296.37	^{29}SiS?	57–56
33.867	57.8 ± 5.4	33.854 ± 0.008	21.0 ± 4.8	33.870	1015.40	295.25	^{30}SiO?	24–23

SUPPORTING INFORMATION

Additional Supporting Information may be found in the online version of this article:

Table A2. VY CMa line fluxes (F) and identifications (IDs) in the SPIRE FTS SLW spectra.
Table A3. VY CMa: Line fluxes and identifications in the SPIRE FTS SSW spectra.

(http://mnras.oxfordjournals.org/lookup/suppl/doi:10.1093/mnras/stt1906/-/DC1).

Please note: Oxford University Press are not responsible for the content or functionality of any supporting materials supplied by the authors. Any queries (other than missing material) should be directed to the corresponding author for the article.

This paper has been typeset from a TEX/LATEX file prepared by the author.